Large-Area and Flexible Plasmonic Metasurface for Laser–Infrared Compatible Camouflage

7 authors, including:

Liming Yuan
Beihang University (BUAA)
53 PUBLICATIONS   **587** CITATIONS

Some of the authors of this publication are also working on these related projects:

Project   designing the scale absorbing materials View project

RESEARCH ARTICLE

Large-Area and Flexible Plasmonic Metasurface for Laser–Infrared Compatible Camouflage

Jingkai Huang, Yuetang Wang, Liming Yuan, Cheng Huang,* Jianming Liao, Chen Ji, and Xiangang Luo*

Due to interminable surveillance and reconnaissance through various sophisticated multispectral detectors, the need for multispectral compatible camouflage is now more than ever. Here, a flexible plasmonic metasurface is proposed to simultaneously realize low reflection at representative lasers (i.e., 1.06, 1.55, and 10.6 μm) and low emission in the atmosphere windows of both 3–5 and 8–14 μm. High absorption for both 1.06 and 1.55 μm lasers is realized by the destructive-interference design of the multilayer Au/Ge/Ti/Ge films, while low reflection for the 10.6 μm laser results from the coding metasurface design, and low emission is attributed to ultrahigh reflection of the continuous Au/Ge/Ti/Ge films in the atmosphere windows. As a proof of concept, a flexible metasurface sample (10 cm × 10 cm) is prepared by the soft-lithography technology. The measured specular reflectivities are 0.017, 0.13, and 0.17 at wavelengths 1.06, 1.55, and 10.6 μm, respectively. Meanwhile, the average emissivities are 0.19 and 0.11 in 3–5 and 8–14 μm, respectively. Additionally, the flexible metasurface also exhibits integrated advantages including easy mass fabrication, good mechanical flexibility and robustness, super-hydrophobic characteristic, unambiguously demonstrating the success of the design strategy for promoting multispectral compatible camouflage.

1. Introduction

Camouflage technology can effectively conceal the signature from objects and render them invisible from the potential threats, such as laser radar,[1–3] infrared camera,[4–10] microwave radar,[11–15] and so on. Particularly, due to the extensive existences of the surveillance system using infrared signal to search for and track a target, infrared camouflage has attracted increasing interest. It is well known that an object with a temperature higher

than the absolute zero can generate infrared emission owing to random energy level transitions in matter.[16,17] According to the Stefan–Boltzmann law, the intensity of the infrared signal emitted from an object is proportional to the surface emissivity and fourth power of its absolute temperature. Therefore, infrared camouflage can be realized through controlling the surface emissivity as well as the temperature.[4,15,18–21] By contrast, controlling the surface emissivity is an easier way to suppress the infrared signal for the reason that it is usually expensive and complicated for the temperature control, which requires additional cooling and heating devices.[2,16,22] Typically, because the background temperature is lower than that of the target,[17] the traditional strategy is to utilize the material with natural high-reflection property to shield the infrared emission. However, due to the fast evolution of multispectral compatible surveillance systems for better object identification, the traditional high-reflection material fails at laser radar, which captures the target by detecting the reflected echo signal.

The wavelengths of the laser commonly used for ranging and guidance include 1.06, 1.55, and 10.6 μm.[1–3,23,24] In order to suppress the power of the echo signal, the camouflage material should have low reflection at laser–radar working wavelengths, which is contradicted with the principle of the infrared camouflage. Hence, it is still an open problem to realize the perfect laser–infrared compatible camouflage, which requires both low reflectivity at the representative laser wavelengths of 1.06, 1.55, and 10.6 μm and low emission in dual-band atmosphere windows of both 3–5 and 8–14 μm. Recently, the emergence of the metasurface, which is composed of subwavelength artificial structures and possesses the capability to effectively manipulate electromagnetic waves, has provided a novel route to address the challenge.[25–32] Qiu and co-workers proposed a simple photonic structure to realize the infrared camouflage compatible with the 10.6 μm laser.[2] Park et al. proposed a multispectral selective absorber based on the single port grating resonance,[24] achieving infrared camouflage compatible with the 1.06 μm laser. Luo and co-workers designed an all-metallic plasmonic metasurface,[33] which has low emissivity in the atmosphere windows and

J. Huang, Y. Wang, L. Yuan, C. Huang, J. Liao, C. Ji, X. Luo
State Key Laboratory of Optical Technologies on Nano-Fabrication and
Micro-Engineering, Institute of Optics and Electronics
Chinese Academy of Sciences
Chengdu 610209, China
E-mail: huangc@ioe.ac.cn; lxg@ioe.ac.cn
J. Huang, C. Huang, J. Liao, X. Luo
School of Optoelectronics
University of Chinese Academy of Sciences
Beijing 100049, China

The ORCID identification number(s) for the author(s) of this article can be found under https://doi.org/10.1002/lpor.202200616

DOI: 10.1002/lpor.202200616

**ADVANCED
SCIENCE NEWS**

www.advancedsciencenews.com
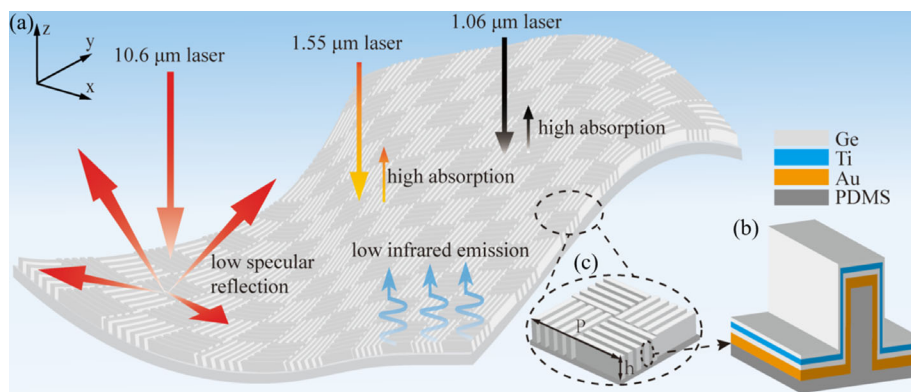
LASER
& PHOTONICS
REVIEWS

www.lpr-journal.org

Figure 1. Schematic diagram of our flexible laser–infrared compatible camouflage metasurface. a) Our design exhibits high absorption for the 1.06 and 1.55 μm lasers, low reflection for the 10.6 μm laser resulting from the coding metasurface composed of orthogonal plasmonic gratings, and low infrared emission attributed to the continuous Au/Ge/Ti/Ge films with ultrahigh reflection over the range from 3 to 14 μm. b) Cross-sectional view of the basic grating element. c) Subgroup element composed of 2×2 orthogonal coding units.

realizes ultralow specular reflection for the 10.6 μm laser by splitting the reflected energy into multiple directions. Despite the fact that these efforts achieve the laser–infrared compatible camouflage, they are mainly intended to work for a single laser. 1D photonic crystal is another method for realizing the laser–infrared compatible camouflage.[1,34] However, they are constrained by low efficiency, small tolerance, and poor stability. Additionally, it is very important to achieve flexible camouflage material for adapting to the random surface in practical applications.[35–37] Conventionally, there are two ways to realize the flexibility: i) using flexible material in each component;[19,36,38] and ii) changing the structure to reduce the mechanical stress.[35,39] However, there still exists much challenge in the fabrication of the flexible material with meticulous structures.

In this paper, a flexible metasurface combined with ultrathin multilayer films is proposed to simultaneously realize the laser (including 1.06, 1.55, and 10.6 μm) and infrared camouflage, which has high absorption for both 1.06 and 1.55 μm lasers by the destructive-interference design of the multilayer Au/Ge/Ti/Ge films, low specular reflection for the 10.6 μm laser resulting from the coding metasurface design, and low infrared emission attributed to the continuous Au/Ge/Ti/Ge films with ultrahigh reflection over the range from 3 to 14 μm. As a proof-of-concept demonstration, the flexible metasurface was prepared by the soft-lithography technology, which has great potential for large-area and low-cost fabrication. We also fully investigated its output performance. Experimental results reveal that our flexible metasurface not only has outstanding performances for the laser–infrared compatible camouflage, but also exhibits integrated advantages including easy mass fabrication, good mechanical flexibility and robustness, super-hydrophobic characteristic, demonstrating the success of the strategy for promoting multispectral compatible camouflage.

2. Results and Discussion

2.1. Design of the Flexible Metasurface

Figure 1a schematically depicts the working principle of our flexible laser–infrared compatible camouflage metasurface, which

has high absorption for near infrared (NIR) including both 1.06 and 1.55 μm lasers, low specular reflection for the 10.6 μm laser, and low infrared emission in the atmosphere windows of both 3–5 and 8–14 μm. The high absorption for the 1.06 and 1.55 μm lasers is realized by the destructive-interference design of the multilayer Au/Ge/Ti/Ge films, as shown in Figure 1b. However, the NIR absorbing structure remains the high reflectivity over the range from 3 to 14 μm for the reason that the functional Ge/Ti/Ge films are too thin to affect the high-reflection characteristic of the bottom Au layer, meaning low emissivity in the atmosphere windows according to Kirchhoff's law. In order to further reduce the reflection of the 10.6 μm laser, we adopt the strategy of coding metasurface, which can redirect the backward scattering energy into well-defined directions instead of the specular direction. In this study, a grating structure combined with the multilayer Au/Ge/Ti/Ge films is proposed to realize the 180° reflection-phase difference for orthogonally polarized illuminations, and then the camouflage metasurface is constructed by the chessboard-like configuration of orthogonal plasmonic gratings, as shown in Figure 1c. The design procedure mainly includes four aspects, i.e., optimization of the NIR-absorbing structure, design of the initial basic perfect-reflection element, optimization of final basic perfect-reflection element, and design of coding metasurface, as shown in Figure S1 (Supporting Information). In order to realize the large-area and low-cost fabrication of the laser–infrared compatible plasmonic metasurface on the flexible substrate, we employ the soft-lithography technology to transfer the subwavelength grating structure from the rigid silicon substrate to the flexible polydimethylsiloxane (PDMS) substrate, and then deposit the multilayer Au/Ge/Ti/Ge films using magnetron sputtering in sequence.

Figure 2a illustrates the NIR-absorbing structure, which consists of a Ti layer, two Ge dielectric spacers, and a bottom Au reflective layer. The incident wave is mainly absorbed by the Ti layer because of its good optical loss characteristic in the NIR region. Meanwhile, it is worth noting that the thickness of the Ti layer should be smaller than the skin depth, avoiding that high reflection occurs around this position. Due to the high refractive index and the infrared lossless property in the atmosphere windows, Ge is employed as the impedance matching layer to
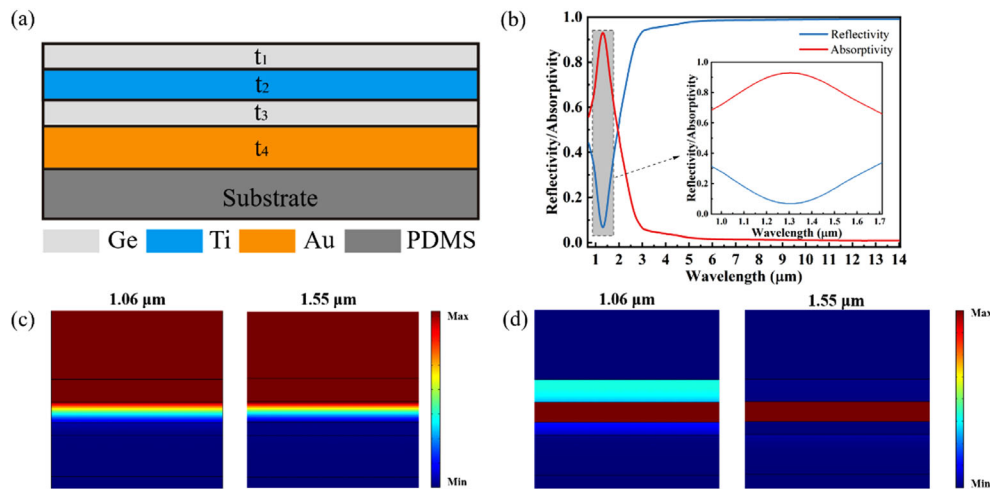
ADVANCED
SCIENCE NEWS
www.advancedsciencenews.com

LASER
& PHOTONICS
REVIEWS

www.lpr-journal.org

Figure 2. a) Schematic of the NIR-absorbing structure. b) Simulation results of the reflection (blue line) and absorption (red line) spectra of the optimized NIR-absorbing structure. Distribution of c) the power flow (W m^{-2}) and d) power loss density (W m^{-3}) in the optimized NIR-absorbing structure for the 1.06 and 1.55 μm lasers, respectively.

minimize total thickness. In order to realize the strong absorption at 1.06 and 1.55 μm as well as high reflectivity in 3–14 μm, the values of t_1, t_2, t_3, and t_4 are optimized to be 28, 25, 16, and 50 nm, respectively. Notably, according to the Euler–Bernoulli beam theory,[40] stiff materials can be bent when their thickness is only a few hundred nanometers.[41] Therefore, the NIR-absorbing structure can meet the requirement for the fabrication of the flexible camouflage. Owing to the tunneling effect of the ultrathin metal, electromagnetic wave can penetrate it and then enter into the lower dielectric layer. A stable oscillation will be formed for the electromagnetic wave of a specific wavelength in the cavity attributed to the existence of the Fabry–Perot resonance. During the repeated oscillation process, the electromagnetic wave will be continuously consumed by the ultrathin loss metal, leading to high-absorption performance. Figure 2b depicts the simulation results of the reflection and absorption spectra of the designed NIR-absorbing structure, showing not only low reflectivity (about 0.2) at both 1.06 and 1.55 μm, but also high reflectivity (>0.9) in 3–14 μm, which means ultralow infrared emissivity (<0.1). In order to further unveil the absorption mechanism, we also simulated the power flow (W m^{-2}) as well as power loss density (W m^{-3}). As shown in Figure 2c, it can be seen that the power flow of the incident waves at both 1.06 and 1.55 μm is uniform in the top Ge layer, rapidly attenuates in the Ti layer, and is close to zero in the middle Ge layer and bottom Au layer. As depicted in Figure 2d and Figure S2 (Supporting Information), it is observed that the power loss of the 1.06 μm laser is mainly concentrated in the Ti layer and partly in the top Ge layer because of its weak loss characteristic in the NIR region, while the power loss at 1.55 μm is mostly concentrated in the Ti layer. Besides, we also investigate the thickness dependence of the reflection spectrum, as shown in Figure S3 (Supporting Information). It can be seen that each layer has enough thickness tolerance for the fabrication. Notably, in the NIR-absorbing structure, the bottom Au layer can be replaced by other metals (e.g., cheaper Al) to reduce the cost, while Ti is thought to be the most reasonable choice for the loss layer, as shown in Figure S4 (Supporting Information).

Generally, there are two ways to reduce the laser echo signal: i) applying absorbing material on the target, which has been adopted for the 1.06 and 1.55 μm lasers in this study; ii) controlling the propagation direction of the echo signal, which will be considered in our camouflage for the CO_2 laser with a wavelength of 10.6 μm. Because the 10.6 μm laser is just in the atmosphere window of 8–14 μm and absorbing materials usually have a specified absorption bandwidth, high absorption at this laser wavelength inevitably enhances the average emission in the infrared camouflage range of 8–14 μm, which violates the infrared camouflage principle. In order to address this issue, the conventional strategy is to utilize an ultranarrow absorbing material working at 10.6 μm. However, the design of the ultranarrow absorbing material always brings forward strict requirements for the practical fabrication due to small tolerance. In our previous work,[33] we have demonstrated a plasmonic metasurface to simultaneously reduce the specular reflection and infrared emission, which redirects the echo signal to a nonthreatening direction instead of absorbing the laser energy. Meanwhile, the structure has a more receptive fabrication tolerance. Herein, we further propose an evolutionary grating structure combined with the NIR-absorbing films, as displayed in the inset of **Figure 3**a. The geometric parameters are optimized as $P_x = 4.5$ μm, $w = 1.4$ μm, and $h = 2.6$ μm, respectively. The thicknesses of the NIR-absorbing films are all identical with those of the planar absorbing films shown in Figure 2a. The simulated reflectivity is more than 90% in 8–14 μm for both transverse electric (TE)- and transverse magnetic (TM)-polarized lights under normal incidence, as depicted in Figure 3a. Meanwhile, Figure 3b shows the relative phase difference between the two polarized lights. It is clearly observed that the phase shift at 10.6 μm is almost 180°. To better explain the behind physical mechanism, Figure 3c,d illustrates the simulated electric field |E| distributions of the grating under the two polarized lights at 10.6 μm. It can be seen that the two orthogonal lights are reflected at different interfaces, i.e., the TE-polarized light cannot penetrate through the grating and reflects at the top surface, while the TM-polarized light is strongly reflected at the bottom of
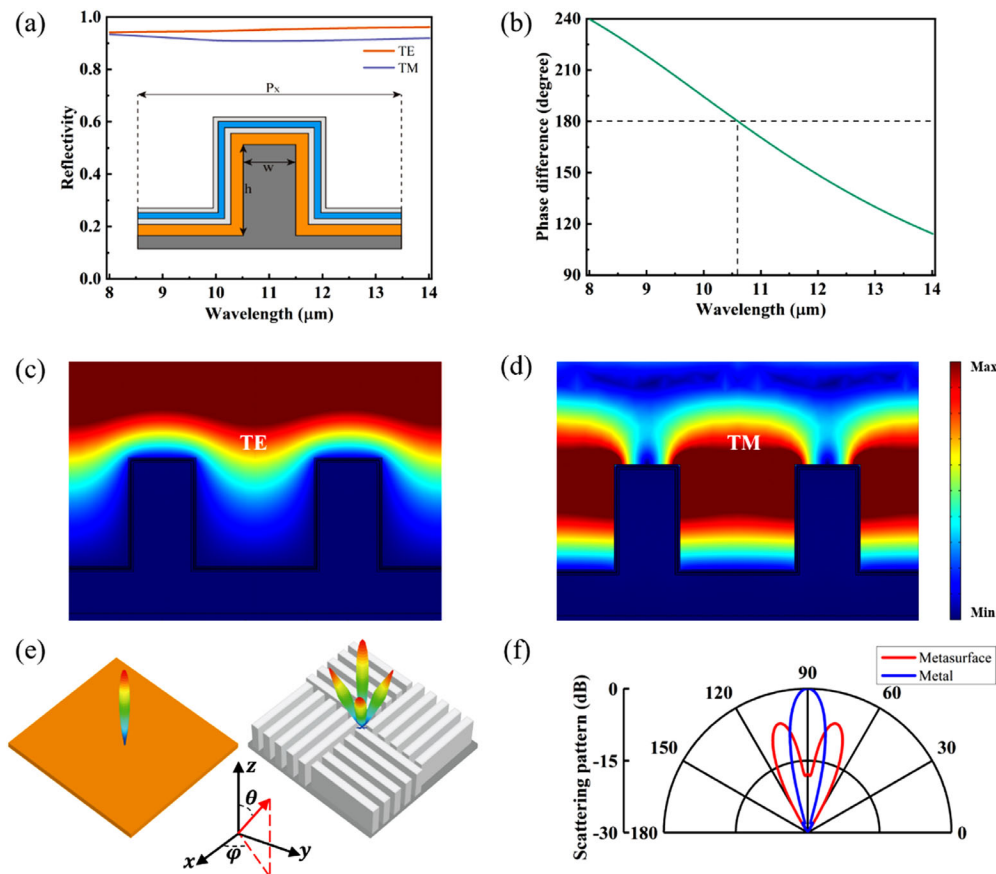
Figure 3. a) Simulated reflection spectra of the basic grating element under TE- and TM-polarized illumination. The inset illustrates the schematic of the basic grating element including the NIR-absorbing structure on the surface. b) Relative phase difference between TM and TE polarizations. The dotted line marked the phase shift at 10.6 µm, which is almost 180°. c,d) Simulated optical field |E| distributions of the basic grating under normal TE- and TM-polarized incidences at 10.6 µm. e) 3D scattering patterns of the metallic plate and the metasurface for normal incidence at 10.6 µm, respectively. f) Scattering patterns in 45° plane for the metasurface and the metallic plate.

the structure due to the plasmonic resonant effect, leading to the phase difference between the reflected TE and TM lights. Furthermore, in order to analyze the influence of the grating structure on the absorbing property of the NIR functional films, we also performed simulations on the power loss density for the evolutionary grating structure, as shown in Figure S5a–d (Supporting Information). The spectra of power loss for each layer are obtained by taking the integral of the power loss density, as shown in Figure S5e,f (Supporting Information). It is clearly observed that the grating structure has little influence on the absorbing performance, even further enhancing the reduction of the specular reflection due to multiple-order reflection effects, as shown in Figure S6 (Supporting Information). Besides, as shown in Figure S7 (Supporting Information), the reflection performance remains stable under various incident angles over the whole range except for 3–5 µm, meaning weakly angle-dependent performance for all lasers and the long-wavelength infrared.

According to the above reflection characteristic of the plasmonic grating, the two orthogonal ones are used as the basic geometrical phase cells to realize the 0 and π reflection phase responses for the coding metasurface design, suppressing the specular reflection of the 10.6 µm laser. To demonstrate this strategy,

we perform full-wave simulations, in which the element composed of 2 × 2 gratings with orthogonal orientations is used with the periodic boundary condition applied to its four sides. Each grating consists of five identical strips, ensuring the resonant wavelength around 10.6 µm. Figure 3e intuitively illustrates the 3D scattering patterns of the metallic plate and the designed metasurface. It is clearly observed that almost all the incident light is reflected into the normal direction by the metallic plate, while the designed metasurface splits the reflected energy into four diagonal directions at the 45° and 135° planes. Figure 3f plots the scattering patterns in 45° plane for the metallic plate and the metasurface. There is 15° deviation between the scattering direction and the normal direction, which is totally consistent with the theoretical value (13.6°). By comparison, the designed metasurface can realize 17.8 dB reflection reduction for the 10.6 µm laser. Besides, according to our simulations on thermal performance, the influences of the ultrathin surface materials and ultrafine surface structure on the heat transfer can be negligible, as shown in Figure S8 (Supporting Information). Hence, our design successfully realizes multilaser (i.e., 1.06, 1.55, and 10.6 µm) and infrared (i.e., 3–5 and 8–14 µm) compatible camouflage functionalities.

**ADVANCED
SCIENCE NEWS**

www.advancedsciencenews.com
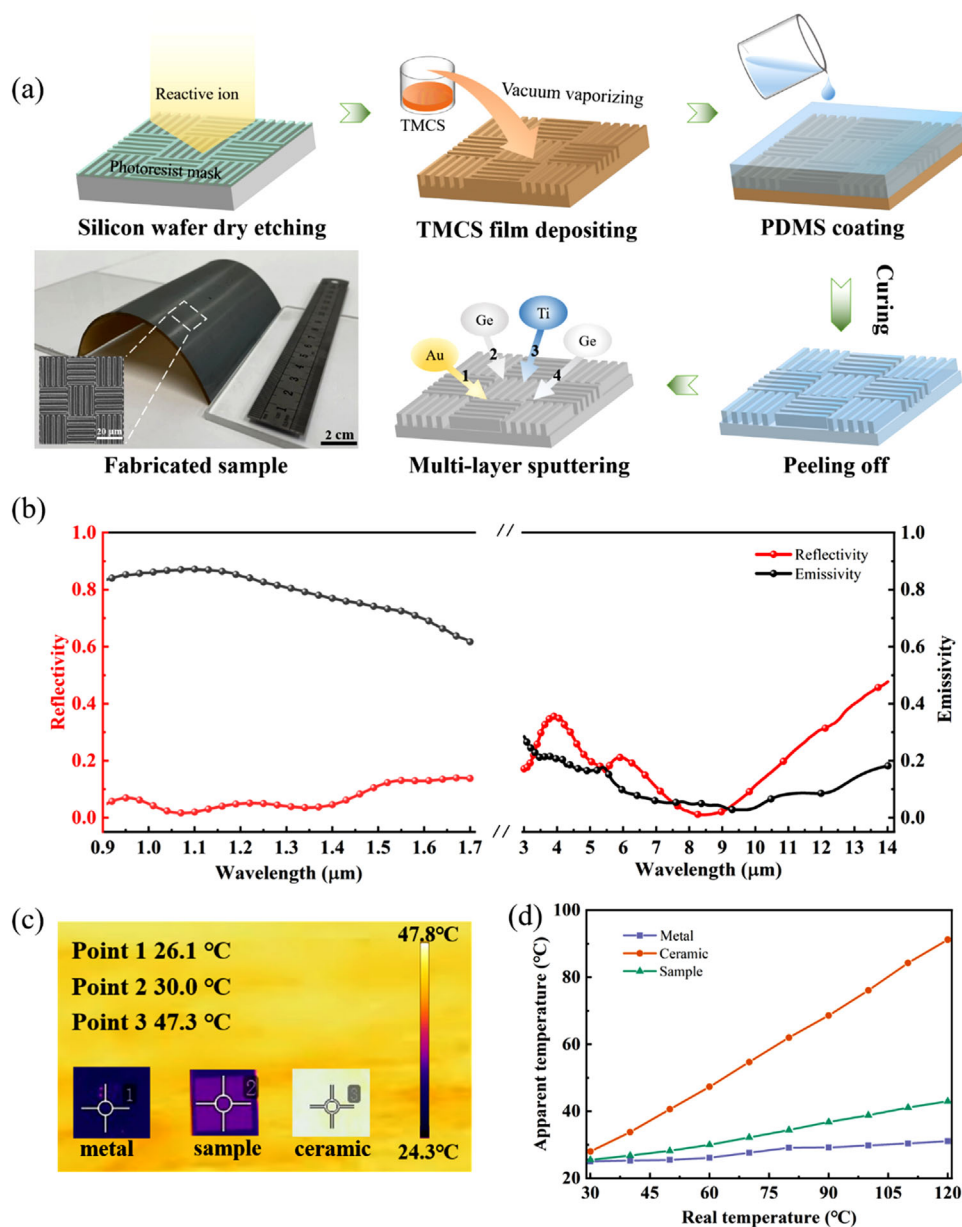
LASER
& PHOTONICS
REVIEWS

www.lpr-journal.org

Figure 4. a) Schematic of the fabrication process of the flexible laser–infrared compatible camouflage metasurface. The inset shows the SEM image of the surface structure of the prepared flexible sample. b) The measured specular reflection (red line) and deduced emission (black line) spectra over the wavelength range of both 0.9–1.7 and 3–14 μm. c) Thermal infrared image of our flexible sample along with a low-emissivity Al foil ($\epsilon \approx 0.05$) and a high-emissivity ceramic wafer ($\epsilon \approx 0.95$) placed on the 60 °C thermostat stage. d) Measured apparent temperatures of our flexible sample, the Al foil, and the ceramic wafer under various heating temperatures.

2.2. Fabrication and Output Performance

To experimentally verify the camouflage performance of our design, we adopt the soft-lithography technology to fabricate the flexible laser–infrared compatible camouflage metasurface according to the optimized parameters. The fabrication processes are schematically illustrated in **Figure 4**a, which mainly include silicon wafer dry etching, surface trimethylchlorosilane (TMCS) treatment, PDMS substrate curing, and multilayer film sputtering; see more details in the "Fabrication" subsection in the Experimental Section. Through this fabrication technology, we achieved

a flexible metasurface sample with a size of 10 cm × 10 cm. The scanning electron microscopy (SEM) image shows that the fabrication technology can perfectly transfer the subwavelength grating structure from the rigid silicon substrate to the flexible PDMS substrate, demonstrating that this fabrication process has a significant potential for the large-area and low-cost fabrication of flexible functional devices with subwavelength structures. Here, along with the measured specular reflectivity, we also utilize the integrating sphere system to measure the total hemispherical directional reflectance, which is used to deduce the emissivity (i.e., the absorptivity) of our opaque sample by $\epsilon = 1 - R$. The

measured specular reflection and deduced emission spectra are plotted in Figure 4b. It can be seen that our sample has very low specular reflectivity values at the laser wavelengths, which are 0.017, 0.13 and 0.17 corresponding to 1.06, 1.55, and 10.6 µm, respectively, validating the good laser camouflage performance of our flexible sample. Meanwhile, the infrared emission is suppressed to the low level over the dual-band atmosphere windows. The average emissivities are 0.19 and 0.11 for the wavelength ranges of 3–5 and 8–14 µm, respectively. It is worth noting that the low specular reflection can be realized over a broad range of around 10.6 µm attributed to abnormal reflection design rather than high-absorption one, indicating more receptive fabrication tolerance. Therefore, it can be concluded that our design paves an effective way for the successful implementation of the compatibility between the laser (especially, the 10.6 µm laser) and the infrared camouflage. To intuitively demonstrate the infrared camouflage performance of our sample, we place it on a thermostat stage along with a low-emissivity Al foil ($\epsilon \approx 0.05$) and a high-emissivity ceramic wafer ($\epsilon \approx 0.95$) for comparison. The infrared image was recorded by an infrared camera as the thermostat stage was heated up to 60 °C, as shown in Figure 4c. Meanwhile, we further measured the apparent temperatures of the three samples under various stage temperatures, as shown in Figure 4d. As can be seen, our flexible sample has a low apparent temperature, which is close to that of the Al foil and obviously lower than that of the ceramic wafer. We also investigated the infrared camouflage performance under different observation angles, as shown in Figure S9 (Supporting Information). It can be seen that the apparent temperature has no significant change when the observation angle increases from 0° to 70°. Meanwhile, it is experimentally demonstrated that our sample is capable of maintaining the infrared camouflage performance in the deformation of twisting and bending (see Figure S10 in the Supporting Information), and the thermal emission from the human body can be totally shielded by our flexible sample (see Figure S11 in the Supporting Information). All these results well validate the great superiority of our flexible metasurface in the infrared camouflage.

Mechanical stability is another important requirement for the practical applications. To validate the stability of our flexible laser–infrared camouflage sample under mechanical deformations, we also performed cycling mechanical tests including bending, twisting, and stretching treatments. In the cycling bending measurement, the ultimate bending diameter was set to 10.5 mm (see the measurement setup in **Figure 5**a). After finishing every 200 bending cycles, we placed our flexible sample on a thermostat stage along with the low-emissivity Al foil and the high-emissivity ceramic wafer, and recorded their apparent temperatures using the infrared camera when the thermostat stage was heated up to 60 °C. As can be seen in Figure 5b, the apparent temperature of our flexible sample has a slight change (less than 2.2 °C). For the cycling twisting measurement, the maximum torsion angle is set to be 90°, as shown in Figure 5c, our flexible sample also exhibits a slight change (no more than 1.7 °C) on the apparent temperature (see Figure 5d). And in the cycling stretching measurement, 20% tensile deformation was applied (see the measurement setup in Figure 5e) referring to the practical application. The change of the apparent temperature does not exceed 2.6 °C for our flexible sample, as shown in Figure 5f. It is worthy pointing out that there is a bit of measurement error due to

the varying ambient temperature, observation angle, data reading position, and so on, which can be demonstrated by the measurement results of the Al foil which has a fluctuation covering 0.5–1.3 °C as well as the ceramic wafer which has a fluctuation covering at 0.5–2.6 °C. Theoretically, the apparent temperature of the Al foil and the ceramic wafer should keep identical for each measurement. Therefore, it can still be concluded that our flexible laser–infrared compatible camouflage metasurface has good mechanical robustness for practical applications. Due to the limit elongation capability of the NIR-absorbing structure (including the Au film), tiny cracks inevitably come to form on the surface of our flexible sample after cycling mechanical treatments, which can be seen from the SEM images in Figure S12 (Supporting Information). For comparison, the specular reflection of our flexible samples after the cycling mechanical treatment has also been re-measured over the wavelength ranges of 0.9–1.7 and 3–14 µm, as shown in Figure 5g,h. It can be seen that the reflection is almost identical with the initial value in 0.9–1.7 µm while it changes slightly in 3–14 µm after different 1000 cycle mechanical treatments. It is believed that our flexible metasurface can adapt well to practical applications with almost no degradation of the laser–infrared compatible camouflage performance under various mechanical treatments.

It is well known that the infrared camouflage low-emissivity effect could easily be compromised by contamination, such as water, which is usually opaque and highly absorptive for the infrared wave, as shown in Figure S13 (Supporting Information). Nevertheless, it is observed that our laser–infrared compatible metasurface also exhibits super-hydrophobic performance, as demonstrated in Figure S14 (Supporting Information). Hence, it can be concluded that our flexible metasurface is capable of resisting the surface contamination from water, which is very beneficial to maintain long-term infrared camouflage performance.

3. Conclusion

In summary, we have proposed a flexible plasmonic metasurface which can simultaneously suppress the reflection at representative laser wavelengths (i.e., 1.06, 1.55, and 10.6 µm) and the emission in the dual-band atmosphere windows (i.e., 3–5 and 8–14 µm). In our strategy, the low reflection for the 1.06 and 1.55 µm lasers is resulted from the strong absorption by the destructive-interference design of the multilayer Au/Ge/Ti/Ge films, while the low reflection for the 10.6 µm laser is implemented by the coding metasurface design, tailoring the wave fronts and redirecting the reflected energy to multiple nonthreatening angles. Meanwhile, the low emission in the atmosphere windows is attributed to the continuous Au/Ge/Ti/Ge films, which have an ultra-high reflection of over the range from 3 to 14 µm. Because the low reflection for the laser (10.6 µm) in the atmosphere window of 8–14 µm is resulting from abnormal reflection design rather than high-absorption one, our metasurface realizes successful implementation of the compatibility between the laser and the infrared camouflage. As a proof of concept, a flexible metasurface sample with a size of 10 cm × 10 cm was prepared by the soft-lithography technology, which has great potential for large-area and low-cost fabrication. Measurement results reveal that the specular reflectivity values are 0.017, 0.13, and 0.17 at the laser wavelengths of 1.06, 1.55, and 10.6 µm, respectively, and the average emissivity
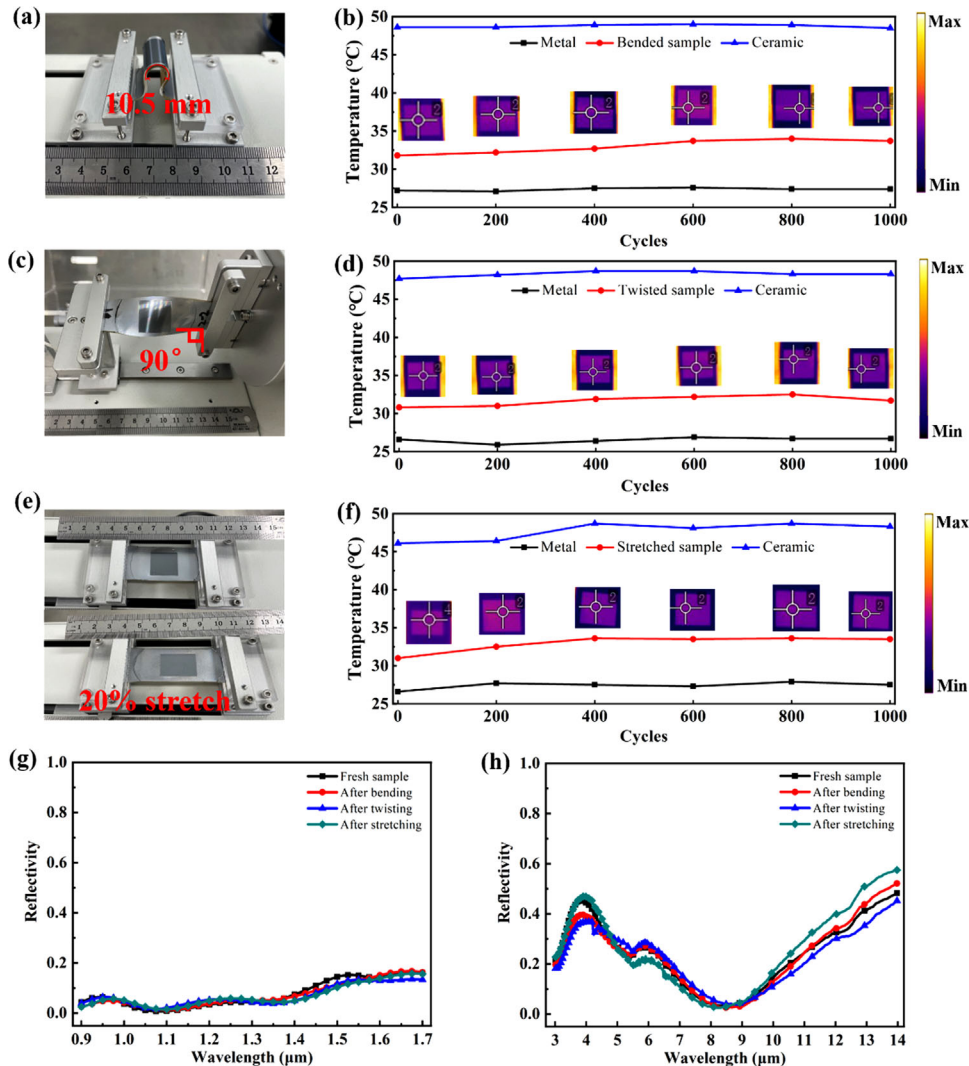
Figure 5. Experimental demonstration of the mechanical stability of our flexible laser–infrared camouflage metasurface. a) Experimental setup of the bending treatment with the ultimate bending diameter of 10.5 mm. b) The apparent temperatures of our flexible sample along with the Al foil and the ceramic wafer measured after every 200 bending cycles. Insets show the infrared photographs of our flexible sample. c) Experimental setup of the twisting treatment with the maximum torsion angle of 90°. d) Measured apparent temperatures after every 200 twisting cycles. e) Experimental setup of stretching treatment with 20% tensile deformation. f) Measured apparent temperatures after every 200 stretching cycles. In the measurement of the apparent temperature, all samples were placed on the 60 °C thermostat stage. g,h) Measurement results of the specular reflection of our flexible samples after 1000 cycle mechanical treatment over the wavelength range of g) 0.9–1.7 µm and h) 3–14 µm.

values are 0.19 and 0.11 in 3–5 and 8–14 µm, respectively. Additionally, we also performed cycling mechanical tests including bending, twisting, and stretching treatments, demonstrating that our flexible metasurface possesses excellent camouflage stability for practical applications. By comparison, our flexible metasurface not only has outstanding performances for the laser–infrared compatible camouflage (see Figure S15 in the Supporting Information), but also exhibits integrated advantages including easy mass fabrication, good mechanical flexibility and robustness, and super-hydrophobic characteristic, showing significant potentials for practical applications. Thus, our work paves an effective way to promote multispectral compatible materials, which may find much potential application in multispectral camouflage and stealth fields.

4. Experimental Section

Simulation: The commercial software COMSOL Multiphysics was employed to perform numerical simulations on the reflection/absorption properties of the multilayer Au/Ge/Ti/Ge films. Periodic boundary conditions were applied along the *x*-direction, while the open boundary condition was used along the *y*-direction. Polarized incident light propagating along the negative *y*-direction illuminated the structure with the electric component perpendicular or parallel to the *xy* plane for the TE or TM polarization. Perfectly matched layers (PMLs) were applied at the top and bottom of the modeling domain to eliminate nonphysical reflections. Optical constants of materials used in the simulations were modeled by fitting optical data of gold,[42] germanium,[43] and titanium.[44] Numerical simulations on the scattering property of the metasurface were performed with commercial software CST Microwave Studio. Unit-cell boundary conditions were used to consider the mutual coupling of adjacent elements.

Fabrication: To experimentally investigate the out performance of the laser–infrared compatible camouflage, a flexible metasurface with the size of 10 cm × 10 cm was fabricated by the soft-lithography technology. First, a 500 nm thick photoresist AZ1500 was coated on a 0.4 mm thick silicon wafer. Then the inverted grating patterns were transferred onto the photoresist through laser direct writing. After developing, the photoresist patterns were etched into the silicon wafer using reactive ion etching to form the desired template with CHF_3. After removing the photoresist with O_2 plasma and acetone, the etched silicon wafer and appropriate TMCS liquid were put into a glass dryer under vacuum for 30 min. Subsequently, the silicon template was washed with alcohol and dried with N_2 gas. In the flexible substrate transfer process, PDMS (SYLGARD 184, Dow Corning) and its curing agent were uniformly mixed together under a mass ratio of 10:1. Then the precursor solution was vacuumed for 20 min at room temperature to remove bubbles. Afterward, the precursor solution was poured onto the silicon template and cured at 80 °C for 2 h in a vacuum chamber. Until the temperature cooled down to ambient temperature, the PDMS substrate was peeled off completely. Finally, Au, Ge, Ti, and Ge films were sputtered on the PDMS substrate sequentially with the corresponding thicknesses of 50, 16, 25, and 28 nm to finish the fabrication of the flexible laser–infrared compatible camouflage metasurface. In the fabrication process, the sputtering rates of Ti, Au, and Ge were 2.9, 4.5, and 3.7 Å s^{-1}, respectively, and the total thickness error could be controlled within 5 nm.

Measurement: The reflection in the range of 0.9–1.7 µm was measured using a spectrophotometer (Lambda 1050, PerkinElmer) under the minimal specular angle of 8°, while the specular reflection and the total hemispherical directional reflectance were respectively obtained by the IR Fourier Spectrometer (VERTEX80, Bruker) and the integrating sphere system (Nicolet iS50, Thermo Fisher) in the range of 3–14 µm. Thermal infrared images were recorded by FLIR T650sc with a spectral range of 7.5–13.0 µm. The microstructure morphology of the flexible metasurface sample was characterized by a scanning electron microscope (SU8010, Hitachi). The cycling mechanical experiments were performed on a mechanical testing platform (FT2000, Shanghai Mifang Electronic Technology Co., Ltd.), in which, the speeds were 15 mm s^{-1}, 40° s^{-1} and 10 mm s^{-1} for the cycling bending, twisting, and stretching tests, respectively.

Supporting Information

Supporting Information is available from the Wiley Online Library or from the author.

Conflict of Interest

The authors declare no conflict of interest.

Data Availability Statement

The data that support the findings of this study are available from the corresponding author upon reasonable request.

[1] H. Zhu, Q. Li, C. Tao, Y. Hong, Z. Xu, W. Shen, S. Kaur, P. Ghosh, M. Qiu, *Nat. Commun.* **2021**, *12*, 1805.

[2] M. Pan, Y. Huang, Q. Li, H. Luo, H. Zhu, S. Kaur, M. Qiu, *Nano Energy* **2020**, *69*, 104449.

[3] X. Feng, M. Pu, F. Zhang, R. Pan, S. Wang, J. Gong, R. Zhang, Y. Guo, X. Li, X. Ma, X. Luo, *Adv. Funct. Mater.* **2022**, *32*, 2205547.

[4] Y. Peng, Y. Li, P. Cao, X. Zhu, C. Qiu, *Adv. Funct. Mater.* **2020**, *30*, 2002061.

[5] Y. Li, X. Bai, T. Yang, H. Luo, C.-W. Qiu, *Nat. Commun.* **2018**, *9*, 273.

[6] H. Zhu, Q. Li, C. Zheng, Y. Hong, Z. Xu, H. Wang, W. Shen, S. Kaur, P. Ghosh, M. Qiu, *Light Sci. Appl.* **2020**, *9*, 60.

[7] E. M. Leung, M. Colorado Escobar, G. T. Stiubianu, S. R. Jim, A. L. Vyatskikh, Z. Feng, N. Garner, P. Patel, K. L. Naughton, M. Follador, E. Karshalev, M. D. Trexler, A. A. Gorodetsky, *Nat. Commun.* **2019**, *10*, 1947.

[8] C. Xu, G. T. Stiubianu, A. A. Gorodetsky, *Science* **2018**, *359*, 1495.

[9] O. Salihoglu, H. B. Uzlu, O. Yakar, S. Aas, O. Balci, N. Kakenov, S. Balci, S. Olcum, S. Süzer, C. Kocabas, *Nano Lett.* **2018**, *18*, 4541.

[10] X. Tao, D. Liu, T. Liu, Z. Meng, J. Yu, H. Cheng, *Adv. Funct. Mater.* **2022**, *32*, 2202661.

[11] C. Huang, J. Yang, C. Ji, L. Yuan, X. Luo, *Small Methods* **2021**, *5*, 2000918.

[12] C. Huang, C. Ji, B. Zhao, J. Peng, L. Yuan, X. Luo, *Adv. Mater. Technol.* **2021**, *6*, 2001050.

[13] T. Kim, J. Bae, N. Lee, H. H. Cho, *Adv. Funct. Mater.* **2019**, *29*, 1807319.

[14] X. Xie, M. Pu, Y. Huang, X. Ma, X. Li, Y. Guo, X. Luo, *Adv. Mater. Technol.* **2019**, *4*, 1800612.

[15] L. Yuan, C. Huang, J. Liao, C. Ji, J. Huang, Y. Wang, X. Luo, *Adv. Sci.* **2022**, *9*, 2201054.

[16] H. Wei, J. Gu, F. Ren, L. Zhang, G. Xu, B. Wang, S. Song, J. Zhao, S. Dou, Y. Li, *Small* **2021**, *17*, 2100446.

[17] R. Hu, W. Xi, Y. Liu, K. Tang, J. Song, X. Luo, J. Wu, C.-W. Qiu, *Mater. Today* **2021**, *45*, 120.

[18] Y. Qu, Q. Li, L. Cai, M. Pan, P. Ghosh, K. Du, M. Qiu, *Light Sci. Appl.* **2018**, *7*, 26.

[19] Y. Huang, B. Ma, A. Pattanayak, S. Kaur, M. Qiu, Q. Li, *Laser Photonics Rev.* **2021**, *15*, 2000391.

[20] Z. Xu, Q. Li, K. Du, S. Long, Y. Yang, X. Cao, H. Luo, H. Zhu, P. Ghosh, W. Shen, M. Qiu, *Laser Photonics Rev.* **2020**, *14*, 1900162.

[21] H. Fang, W. Xie, X. Li, K. Fan, Y.-T. Lai, B. Sun, S. Bai, W. J. Padilla, P.-C. Hsu, *Nano Lett.* **2021**, *21*, 4106.

[22] X. Liu, W. J. Padilla, *Adv. Mater.* **2016**, *28*, 871.

[23] X. Feng, X. Xie, M. Pu, X. Ma, Y. Guo, X. Li, X. Luo, *Opt. Express* **2020**, *28*, 9445.

[24] C. Park, J. Kim, J. W. Hahn, *Adv. Opt. Mater.* **2021**, *9*, 2002225.

[25] X. Luo, *Sci. China Phys. Mech. Astron.* **2015**, *58*, 594201.

[26] N. Yu, F. Capasso, *Nat. Mater.* **2014**, *13*, 139.

[27] X. Ma, M. Pu, X. Li, Y. Guo, X. Luo, *Opto-Electron. Adv.* **2019**, *2*, 18002301.

[28] J. Deng, Z. Li, J. Li, Z. Zhou, F. Gao, C. Qiu, B. Yan, *Adv. Opt. Mater.* **2022**, *10*, 2200949.

[29] K. Dou, X. Xie, M. Pu, X. Li, X. Ma, C. Wang, X. Luo, *Opto-Electron. Adv.* **2020**, *3*, 19000501.

[30] N. Yu, P. Genevet, M. A. Kats, F. Aieta, J.-P. Tetienne, F. Capasso, Z. Gaburro, *Science* **2011**, *334*, 333.

[31] H. Gao, H. Fan, W. Xiong, M. Hong, *Opto-Electron. Adv.* **2021**, *4*, 210030.

[32] J. Deng, L. Deng, Z. Guan, J. Tao, G. Li, Z. Li, Z. Li, S. Yu, G. Zheng, *Nano Lett.* **2020**, *20*, 1830.

[33] X. Xie, X. Li, M. Pu, X. Ma, K. Liu, Y. Guo, X. Luo, *Adv. Funct. Mater.* **2018**, *28*, 1706673.

[34] J.-K. Zhang, J.-M. Shi, D.-P. Zhao, Q.-C. Wang, C.-M. Wang, *Infrared Phys. Technol.* **2017**, *85*, 62.

[35] N. Lee, J. Lim, I. Chang, H. M. Bae, J. Nam, H. H. Cho, *Adv. Opt. Mater.* **2022**, *10*, 2200448.

[36] L. Xiao, H. Ma, J. Liu, W. Zhao, Y. Jia, Q. Zhao, K. Liu, Y. Wu, Y. Wei, S. Fan, K. Jiang, *Nano Lett.* **2015**, *15*, 8365.

[37] J. Ahn, T. Lim, C. S. Yeo, T. Hong, S.-M. Jeong, S. Y. Park, S. Ju, *ACS Appl. Mater. Interfaces* **2019**, *11*, 14296.

[38] C. Zhang, X. Wu, C. Huang, J. Peng, C. Ji, J. Yang, Y. Huang, Y. Guo, X. Luo, *Adv. Mater. Technol.* **2019**, *4*, 1900063.

[39] N. Lee, J.-S. Lim, I. Chang, D. Lee, H. H. Cho, *ACS Appl. Mater. Interfaces* **2021**, *13*, 43524.

[40] O. A. Bauchau, J. I. Craig, *Structural Analysis: With Applications to Aerospace Structures*, Springer, Dordrecht **2009**.

[41] J. Wang, B. Xiong, R. Peng, C. Li, B. Hou, C. Chen, Y. Liu, M. Wang, *Small* **2021**, *17*, 2101282.

[42] R. L. Olmon, B. Slovick, T. W. Johnson, D. Shelton, S.-H. Oh, G. D. Boreman, M. B. Raschke, *Phys. Rev. B* **2012**, *86*, 235147.

[43] T. N. Nunley, N. S. Fernando, N. Samarasingha, J. M. Moya, C. M. Nelson, A. A. Medina, S. Zollner, *J. Vac. Sci. Technol., B: Nanotechnol. Microelectron.: Mater., Process., Meas., Phenom.* **2016**, *34*, 061205.

[44] M. A. Ordal, R. J. Bell, R. W. Alexander, L. A. Newquist, M. R. Querry, *Appl. Opt.* **1988**, *27*, 1203.